Chapter 4:
Spatial and Temporal CO$_2$ Change in Indian Context

This chapter elaborates the portion of the present work carrying out the spatial distribution of the atmospheric column averages of carbon dioxide (CO$_2$) retrieved at different places of India from Next Generation Airborne Visible Infrared Spectrometer (AVIRIS-NG) image analysis. An overall picture of long-term CO$_2$ change in India is obtained with the data of NASA Giovanni online environment. The CO$_2$ column average values retrieved for the sites of varied CO$_2$ source and sink potentials revealed a balanced condition of anthropogenic emission and vegetative sequestration. The temporal change informed of a steady linear increase for the past two decades.

This work also establishes two other significant application of AVIRIS-NG images. The first one is the assessment of the spatial distribution of atmospheric water vapour comparing two consecutive CO$_2$ absorption bands. This is authenticated by comparing the original data available with the data source. The other one is the suitability of detecting point sources of carbon dioxide (CO$_2$) from the images, which is validated by comparing spatial CO$_2$ distribution at Jharia coalfield, a region of high CO$_2$ density, with that at nearby urban regions.

4.1. Stimulus to the Work

The assessment of atmospheric CO$_2$ with remote sensors is a well-known topic. Nevertheless, as reviewed in Chapter 2, the assessment of CO$_2$ in the tropical atmosphere of India has several distinctions by virtue of the large area, dense population, high demand of fossil fuels and diversified environmental features including the widespread vegetated regions and surrounding seas.

The general purpose airborne hyperspectral sensor named Airborne Visible Infrared Spectrometer (AVIRIS) (Green et al. 1998) and its next generation version (AVIRIS-NG) (Chapman et al. 2019) have an extensive inheritance of efficaciously assessing the local concentrations of atmospheric CO$_2$ (Green 2001, Spinetti et al. 2008, Dennison et al. 2013) and other greenhouse gases (Thorpe et al. 2017). As mentioned in Chapter 3, AVIRIS-NG flights over different places of India were conducted for the first time in 2015-16 and in 2018 jointly by Space Applications Centre, Indian Space Research

organization (ISRO), Govt. of India and Jet Propulsion Laboratory, National Aeronautics and Space Administration (NASA). The opportunity for accessing the AVIRIS-NG images resulted in various studies on different natural and man-made features summarized in literature (Green et al. 2017, Bhattacharya et al. 2019). The present work has availed of the prospect of the AVIRIS-NG image resource for retrieving the spatial trend of CO$_2$ in different environments of India. It has estimated a gross long term change of CO$_2$ in India from NASA Giovanni open data source, retrieved the spatial variation of CO$_2$ from AVIRIS-NG data for places of varying emission and sequestration potential and compared those with the contemporary results obtained from Orbiting Carbon Observatory-2 (OCO-2), a global CO$_2$ sensor.

4.2. Data and Methodology

The study objective was to first draw a broad picture of long-term CO$_2$ change across the Indian atmosphere, and then to sketch the current CO$_2$ mapping generated from AVIRIS-NG images. For this reason, the majority of India's mainland was divided into five overlapping rectangular zones, as shown in Table 4.1. For analysis, nine particular areas covered by AVIRIS-NG imaging were chosen (Table 4.1 and Figure 4.1). The selection of these locations, namely **A** through **I**, was at random, but the difference of geographic and environmental aspects was considered with the anticipation of a wide range of CO$_2$ source and sink.

4.2.1. Open-Source CO$_2$ Data Procurement

NASA-Giovanni v4.34 online environment (https://giovanni.gsfc.nasa.gov/79pprox.79/) was used to collect time series, area-averaged values of monthly average CO$_2$ mole fraction (ppm) derived from Atmospheric Infrared Sounder (AIRS) for two consecutive periods of 2003–2011 and 2010–2016. For the years 2016 to 2019, the day-wise column-averaged CO$_2$ dry-air mole fraction (ppm) values were extracted from the OCO-2 database (https://oco.jpl.nasa.gov/oco-2-data-center/) produced by the Jet Propulsion Laboratory, California Institute of Technology and archived by the NASA Goddard Earth Science Data and Information Services Centre.

Table 4. 1. The extents of five rectangular regions enclosing a majority of India, as well as the locations of nine Indian sites with contrast environments and expected contrast CO_2 components related to vegetation/biosphere (Bio) and air-sea (Ocean) exchanges, as well as man-made (MM) fossil fuel combustion and fire emission.

The five rectangular regions covering the major portion of India			
Region-1: 22.5 – 27.5 N, 70.0 – 88.5 E Region-2: 11.5 – 31.5 N, 75.0 – 79.0 E Region-3: 20.0 – 26.5 N, 79.0 – 87.5 E Region-4: 24.5 – 26.5 N, 93.0 – 94.5 E Region-5: 21.0 – 24.0 N, 69.5 – 72.5 E			
Specific Sites	Expected CO_2 Components		
	Ocean	Bio	MM
A. Sundarban	High	High	Low
B. Kolkata	High	High	High
C. Jaduguda	Low	High	High
D. Jodhpur	Low	Low	High
E. Jaisalmer	Low	Low	Low
F. Kakinada City	High	Low	High
G. Krusadai Reef Complex	High	Low	Low
H. Madumalai	Low	High	Low
I. Ratnagiri	High	High	Low

Figure 4. 1. Google earth map showing the boundaries (green) of the five overlapping rectangular regions enclosing a major portion of India and the locations of the nine Indian sites specified in Table 4.1.

The available data were categorised into areas of 1°×1° span, encompassing each of sites **A** through **I** (Table 4.1), as well as two deep sea regions near India: one from the Arabian Sea (13°–16° N, 63°–66° E) and one from the Bay of Bengal (13°–16° N, 87°–90° E). These two areas were meant to be the least impacted by human activity. The years 2020 and 2021, as well as the CO$_2$ data obtained from the most recent sensor Orbiting Carbon Observatory-3 during this time period, were purposefully avoided because the pandemic-related global lockdown was discovered to modify the usual annual change of CO$_2$ column average (Raychaudhuri and Roy, 2022), which would not match the current trend discussed in chapter 7.

4.2.2. CO$_2$ from AVIRIS-NG Images

AVIRIS-NG images for sites **A** to **I** (Table 4.1) were obtained from the NASA website (https://avirisng.jpl.nasa.gov/dataportal/). Spatial selections of 500×500 pixels and spectral subsets ranging from band 315 (1.949 µm) to band 349 (2.119 µm) were chosen from each orthocorrected radiance picture file, and sensor heights were recorded in the associated observation file. The two absorption bands, CO$_2$-1 and CO$_2$-2, were identified on the hyperspectral image-derived radiance spectra at roughly 2 µm (Section 3.1.3). The CO$_2$ concentrations were calculated from the absorption depths using the a-DOAS method, which was created in this study and is shown in sections 3.13 and 3.14. There are also the AVIRIS-NG band values for computing mean radiance at absorbing and non-absorbing wavelengths indicated.

4.3. Gross Results on Temporal CO$_2$ Change Over India

The monthly average CO$_2$ mole fraction (ppm) obtained from NASA Giovanni online environment for the five regions of Table 4.1 spanning a large portion of India is plotted in figures 4.2(a) and 4.2(b) for the periods 2003–2011 and 2010–2016, respectively, to give an idea of the overall time variation of CO$_2$.
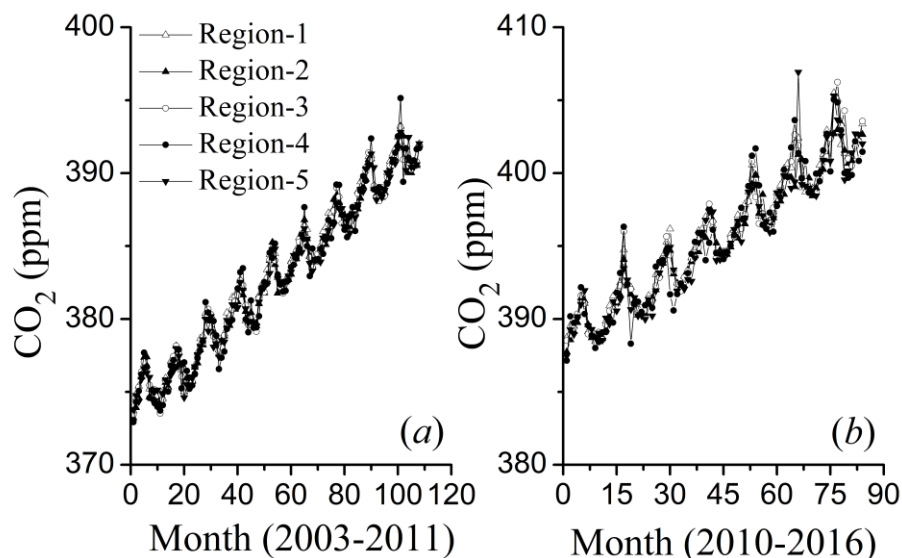
Figure 4. 2. Monthly average CO_2 mole fraction (ppm) obtained from NASA-Giovanni online environment for regions 1 through 5 (Table 4.1): (a) for years 2003–2011 and (b) for years 2010–2016.

Table 4. 2. Time variation of CO_2 concentration in India obtained from Figure 4.2 compared with earlier reports.

Reference	Study area	Data source	Results on CO_2
Bhattacharya et al. (2009)	Cape Rama ≈ 73.9°E, 15.1°N	Gas chromatography of *in situ* air samples	Steady increase within 350–380 ppm 82pprox.. for years 1993–2003 with irregular seasonal fluctuations
Tiwari et al., 2011	-do-	Gas chromatography of *in situ* air samples and model simulation	Steady increase within 350–380 ppm 82pprox.. for years 1993–2002 with seasonal fluctuations, maxima in March-April, minima in October-November
Chhabra and Gohel, 2017	-do-	OCO-2 and CarbonTracker2013B	Steady increase within 373–413 ppm 82pprox.. for years 2000–2015 with irregular seasonal fluctuation
Singh et al., 2015	Average over India and around	AIRS online data (www.mirador. gsfc.nasa.gov)	Steady increase within 375 – 395 ppm approx. for years 2003 – 2011 with irregular seasonal fluctuation
Present work	Average over major portion of India	NASA Giovanni	Steady increase with seasonal fluctuation, maxima in summer (May-June) (i) Years 2003–2011 linear fit: 373.86 to 392.23 ppm, increase @ 2.041 ppm/year (ii) Years 2010–2016 linear fit: 388.43–403.02 ppm, increase @ 2.086 ppm/year (iii) Extrapolation for years 1993–2003 353.62–373.86 ppm

The data points in Figure 4.2(a) and 4.2(b) practically overlap, and there is a seasonal oscillation. The overarching aspect for both successive eras is the continuous growth with time. The results of fitting the aggregate data points with linear and second order polynomials are substantially identical. The linear extrapolation of the current data to the period 1993–2003 matches the earlier reports well, and the current study was determined to be in excellent agreement with the previous reports, as shown in Table 4.2. For the previous three decades, the gross CO_2 column concentration over Indian atmosphere has been growing at a consistent pace of roughly 2 ppm per year. Figure 4.2 and Table 4.2 show an average picture of the history and present situations of air-mixed column averaged CO_2 in the Indian atmosphere. The AVIRIS-NG pictures shown in the next section provide more information on the spatial variances.

4.4. Spatial CO₂ Map from AVIRIS-NG

Figure 4.3 depicts the false colour composite derived from AVIRIS-NG pictures for the surface characteristics of the locations under study. Figure 4.4 depicts the equivalent geographical distribution of CO_2 in these locations as obtained from AVIRIS-NG images using the CO_2-2 absorption band as described in section 2.2. Because the images were obtained at the same time of year 2018 with just a few days difference (except for sites **A** and **H** collected in 2016), Figure 4.4 may be regarded as an extended snapshot of the air-mixed CO_2 situations in India under various environmental circumstances. In varying degrees, the equilibrium of emission and sequestration is represented in these regional distributions.

According to Table 4.1, site **A** (Sunderban) has excellent conditions for both vegetative and marine sequestrations as well as a lower density of human habitat, resulting in low man-made emissions. In the long run, it gives a low CO_2 value. Site **B** (Kolkata), not far from site **A**, has a densely populated metropolitan area and a densely vegetated region. Despite the existence of plants, the resulting CO_2 is high and varies little over the region. Site **C** (Jaduguda), which is located in a separate location with comparable

vegetation and population characteristics as site **B** but lacks the marine sequestering effect, has a somewhat similar range but higher values of CO$_2$ spatial distribution than that in site **B**. The three locations mentioned above depict a balanced state of CO$_2$ under anthropogenic emission and vegetative and/or marine sequestration.
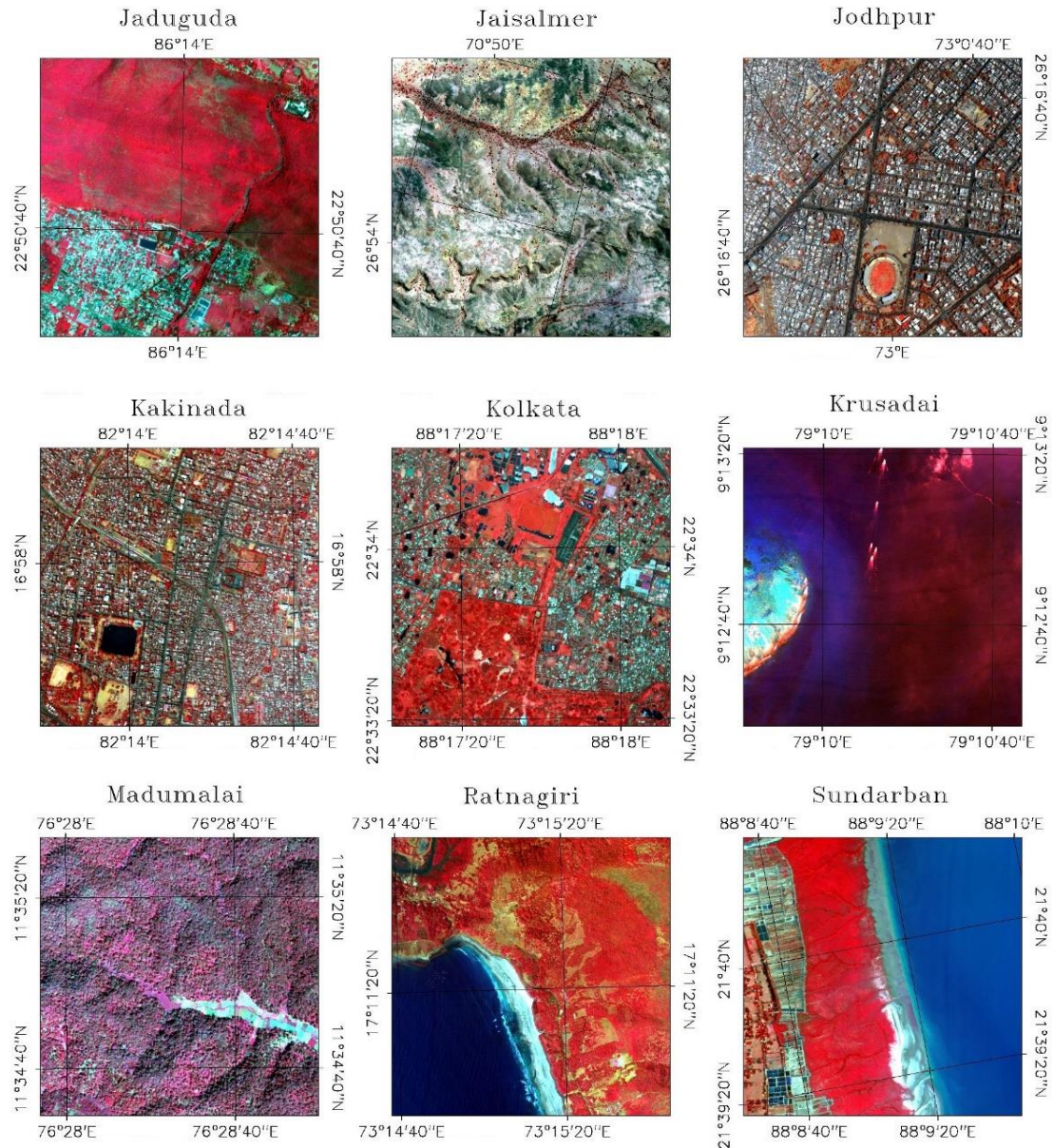

Figure 4. 3. RGB false colour composite for the surface features of sites A through I (Table 4.1) obtained from AVIRIS-NG images.

The next two sites provide a distinct but consistent perspective. Site **D** (Jodhpur) is a densely populated metropolitan area with little greenery and is too distant from the sea. It has a high CO_2 content. Site **E** (Jaisalmer) shares similar natural characteristics but has a lower human density. As a result, the CO_2 concentration is significantly lower than at site **D**.
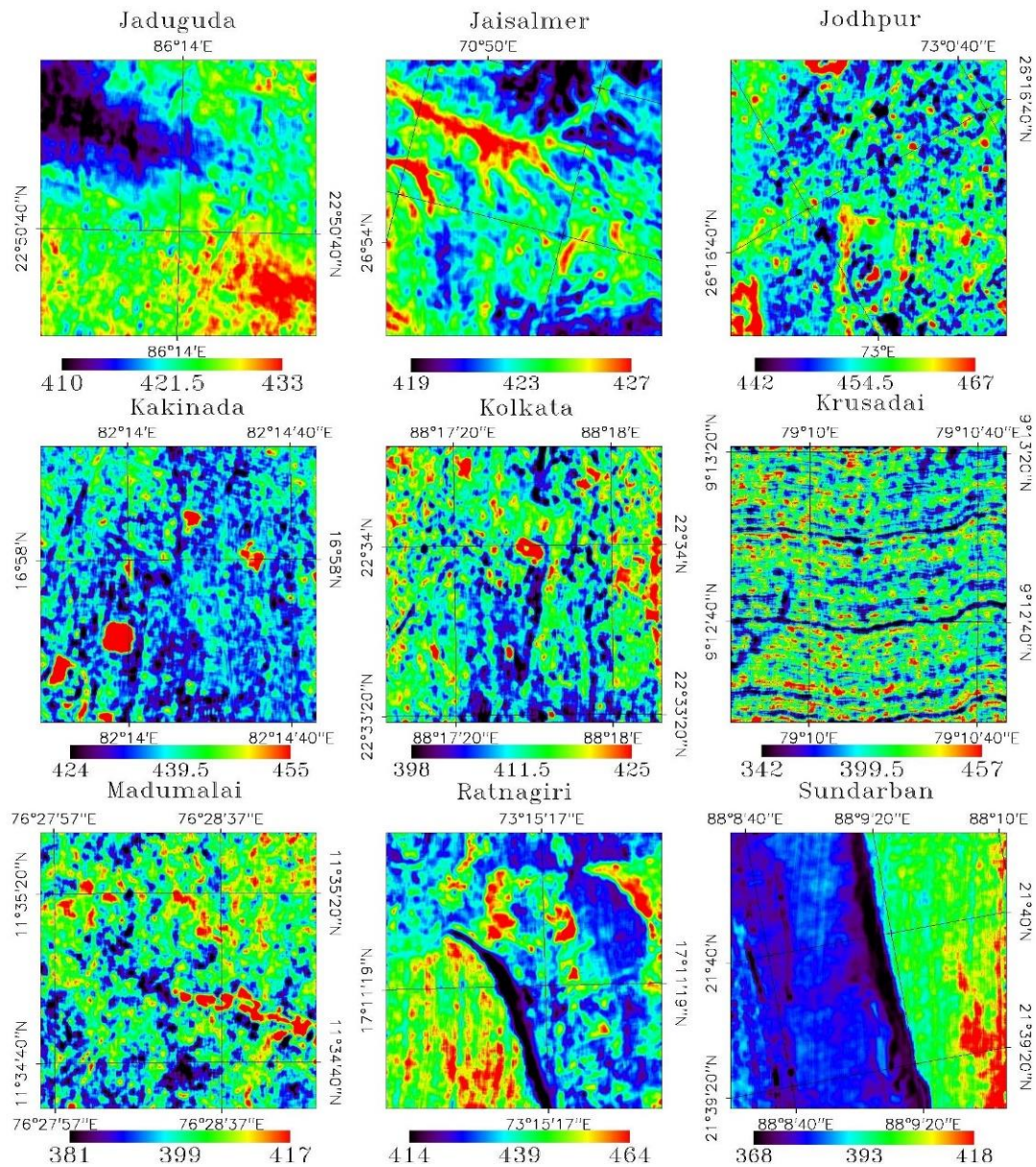

Figure 4. 4. The spatial distribution of CO_2 corresponding to the surface features of the sites of Figure 4.3, retrieved from AVIRIS-NG images using the CO_2-2 absorption band by the method outlined at section 2.2.
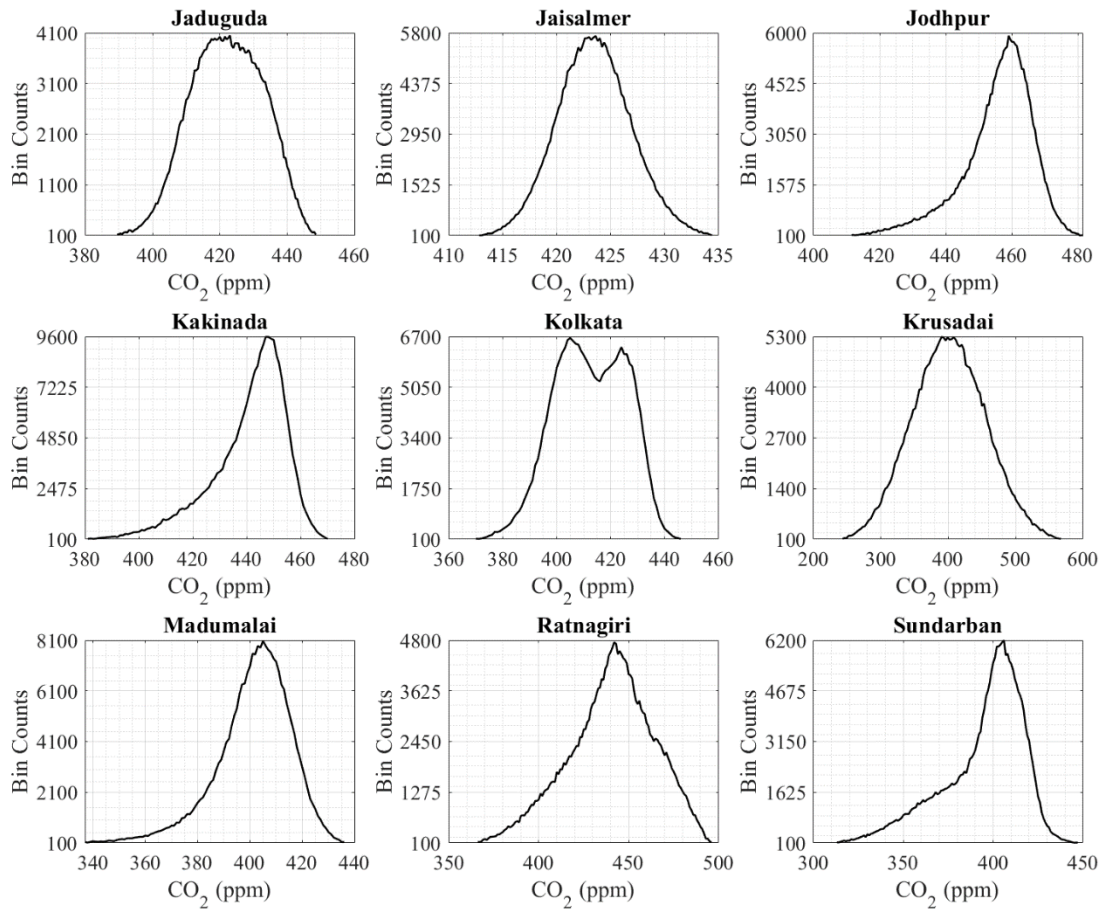
Figure 4. 5. Histogram distribution of CO_2 by the number of pixels corresponding to the sites of Figure 4.4.

The CO_2 profiles of two more locations, site **F** (Kakinada) and site **G** (Krusadai), both near seaside, are now compared. The distinction is that the former is heavily populated, whilst the latter is sparsely populated. The accompanying variation in CO_2 levels is extremely noticeable. Site **G** has significantly lower CO_2 concentrations. What's more, the spatial distribution of CO_2, whatever its value, is uniform throughout the area in both sites. This is due to the fact that the source of emission or sequestration is consistent throughout. Site **H** (Madumalai), which is mostly vegetated, has a comparable homogeneity of CO_2 spatial distribution. Site **I** (Ratnagiri), a comparable coastal location to sites **F** and **A**, has a greater CO_2 value despite having both vegetation and sea as sequestering agents.

The above comparative features can be viewed more quantitatively in Figure 4.5 that presents the corresponding histograms. From Figure 4.5 a common result for the aforementioned locations can be observed. Places endowed in slower sequestering agents like ocean (site F, G, I, A) have the widest histograms or the difference between the maximum and the minimum CO$_2$, compared to the places with faster sequestering agents like vegetation (site H and C). The places with no such agents (site D and E) show the least spread histograms with the peak centered at high CO$_2$ value. The accompanying image of dramatically fluctuating CO$_2$ levels across different parts of India was not taken in a broad view. Indeed, the preceding narrative suggests the sequestering capability in the Indian environment, as evidenced by figures 4.6, 4.7, and 4.8, which are introduced later.

4.5. Balanced Condition of CO$_2$

Figure 4.6(a) depicts the temporal changes of the available daily CO$_2$ data obtained from OCO-2 for the period 2016-19 over a $1° \times 1°$ ($\approx$ 100 km $\times$ 100 km) span surrounding each of the sites **A** through **I**, fitted with straight lines, in order to understand the trends of monotonic changes in CO$_2$ around the above areas in recent years. It is worth noting that, despite the diverse CO$_2$ distribution in different sites (Figure 4.4), the temporal increases for all of them are essentially identical. This is because each little section of Figure 4.4 is mixed up with numerous surrounding characteristics, resulting in an overall uniformity of emission and sequestration. Figure 4.6(b) shows the finer details of the linear increasing slopes (ppm/year) reflecting the rate of CO$_2$ increase in these locations. It has been observed that the effect of slower CO$_2$ growth is still apparent in locations with higher sequestering capability. Table 4.3 compares the current findings to recent reports.
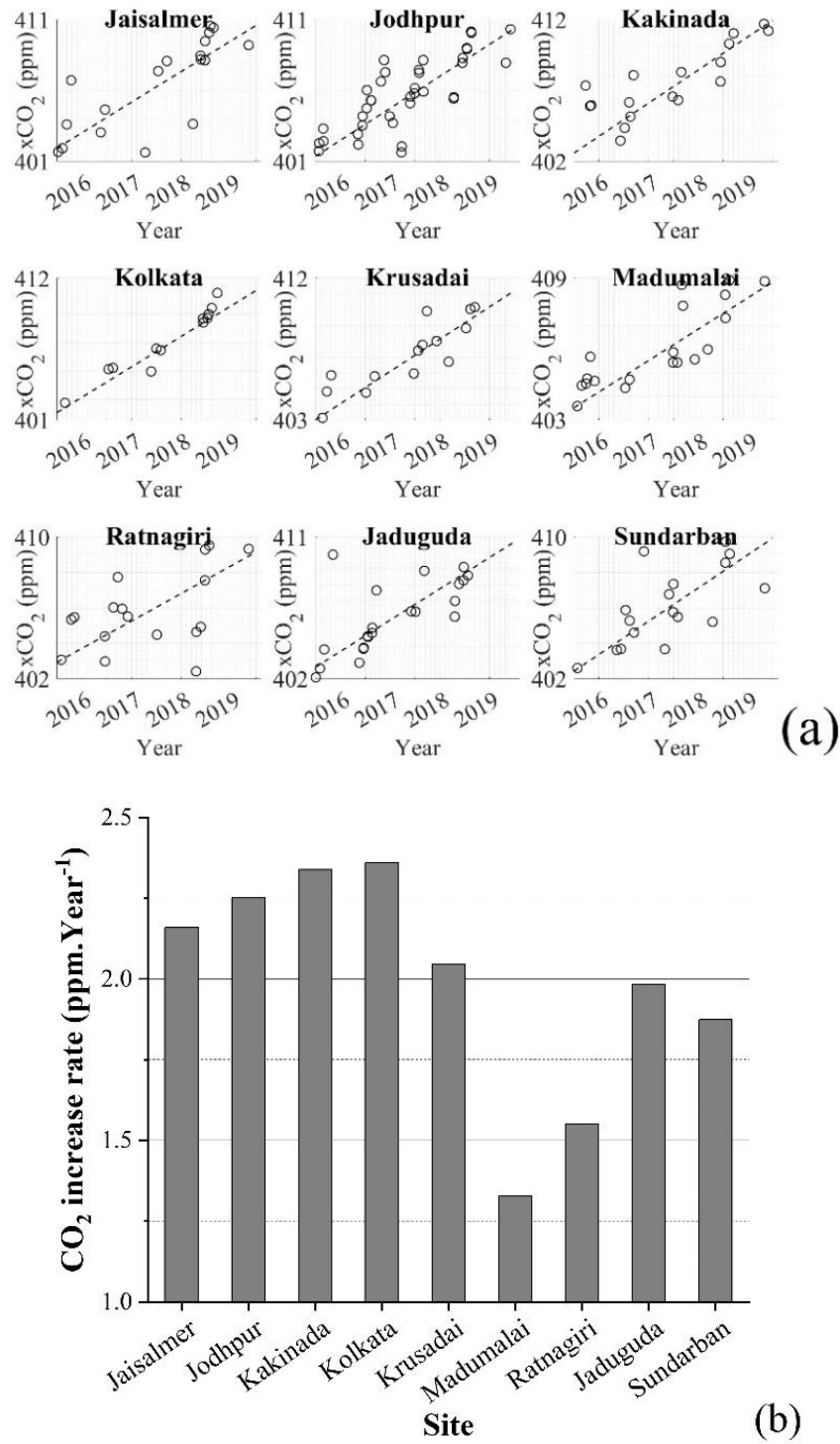
Figure 4. 6. Temporal changes of the CO_2 daily data for the period of 2016-19 over 1°×1° (≈ 100 km × 100 km) area surrounding each of the sites **A** through **I**, (a) fitted with straight lines and (b) the slopes indicating the linear increasing rate (ppm/year).

Table 4. 3. Comparison of present results with earlier reports on the change of column-averaged mixing ratio of CO$_2$.

Reference	Data source	Study area	Results on CO$_2$ relevant to Indian region
Hakkarainen et al. (2016)	OCO-2	Global	Anthropogenic CO$_2$ component: 0–1 ppm (approx.) over India for years 2014–16
Janardanan et al. (2016)	GOSAT (Greenhouse gases Observing SATellite) and other open-source data	Global	Anthropogenic CO$_2$ component: 0.98–2.44 ppm for four urban places of India, observations during 2009–2012
Hakkarainen et al. (2019)	OCO-2	Global	Anthropogenic CO$_2$ component: 1–2 ppm (approx.) over India for years 2015–18 with seasonal increase in summer/monsoon
Present work	OCO-2	Different places of India	Increase of CO$_2$ during 2016 – 2019 at regions of varying natural and man-made features: about 1.5 – 2.3 ppm/year.

Figure 4.7 depicts the fitted curves for CO$_2$ concentration (ppm) of urban locations (Jaduguda, Jodhpur, Kakinada, and Kolkata) (white circles, solid line) compared to deep sea (black circles, dashed line) for the years 2016 to 2019. It is evident that deep-sea locations, which is supposed to be free from human activities, do not always display a reduced extent of CO$_2$, which implies that the sea sequestration of CO$_2$ at a slower rate is insufficient to face the rapidly growing global CO$_2$ levels. The vast amount of greenery spread throughout India resulting the CO$_2$ sequestered by vegetation at faster rate may have allowed the country to compensate for emissions over populous areas and maintain a constant level in atmospheric CO$_2$ augmentation.
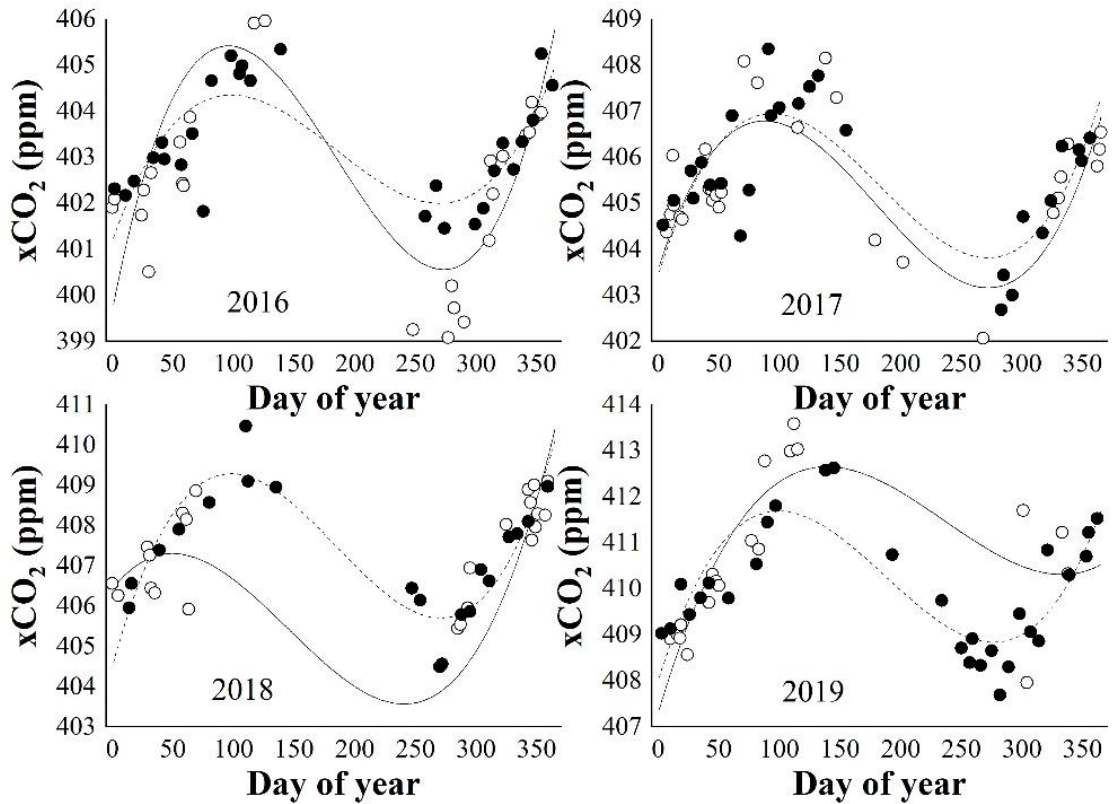
Figure 4. 7. CO_2 concentration (ppm) at urban sites (Jaduguda, Jodhpur, Kakinada and Kolkata), plotted and fitted (white circles, solid line) along with that for deep sea (black circles, dashed line) for years 2016 to 2019.

4.6. Estimating Water Vapour (H_2O)

This part demonstrated another aspect of the AVIRIS-NG picture. Using CO_2 absorption bands, it can determine the geographical distribution of water vapour concentration, which is significant in tropical nations.

Previously (Raychaudhuri and Roy 2021), it was demonstrated that the truncation of one of the CO_2 absorptions, namely CO_2-1, by the nearby water vapour (H_2O) absorption may be corrected by a proportionality constant (R) linked to the two adjacent CO_2 absorption depths. This study, shown in section 3.5, shows how the same effect may be used to reverse track the water vapour concentration using AVIRIS-NG images. Although H_2O and CO_2 are distinct atmospheric variables, they can be associated via R-values, which are dependent on both CO_2 and H_2O concentrations at the same time. This

90

means that a function like $g(CO_2, H_2O) = R$ and hence a function like $f(CO_2, R)=H_2O$ may be generated. To determine the function f, a variety of CO_2 absorption spectra were simulated with MODTRAN6 for varied CO_2 (100-600 ppm) and H_2O (0-10 gcm-2) concentrations and the related R-values were computed. Because MODTRAN6 uses an input of CO_2 concentration to simulate the radiance spectra and has a default observer height of 705 km, the CO_2 values were calculated again using Eq. (3.2) from the MODTRAN6 simulated spectra for all instances by assuming $z = 7.24$ km [Figure 3.1] as the effective optical path length for the reflected region as. These data sets were fitted using a polynomial function based on the assumption that H_2O levels are dependent on CO_2 and R-values.

$$f(x,y) = p_{00} + p_{10}.x + p_{01}.y + p_{20}.x^2 + p_{11}.x.y + p_{02}.y^2 + p_{30}.x^3 + p_{21}.x^2.y + p_{12}.x.y^2 \qquad (4.1)$$

The subscripts of the parameters in Eq. (4.1) denote the power of x and y respectively for their corresponding variables. Knowing the CO_2 and R-values, one can calculate the spatial distribution of H_2O values over the whole region covered by the AVIRIS-NG picture. Figure 4.8(a) depicts the interdependence of R-values, CO_2 and H_2O fluctuation over vast ranges simulated with MODTRAN 6. A two-dimensional polynomial function is used to model the dependency of H_2O on CO_2 and R-values. Figure 4.8(b) depicts the original H_2O distribution supplied with the AVIRIS-NG picture. In terms of proportionate geographic variation, the H_2O spatial distribution retrieval with the current technique for Kolkata (site **B**), shown among the H_2O spatial mappings recovered for all nine sites in Figure 4.9, is found to be in excellent agreement with that of Figure 4.8(b). Another basic aspect of H_2O dispersion is seen in Figure 4.9. Because H_2O is a function of both CO_2 and R, sites with a broad range of CO_2 variation, such as Krusadai, also have a wide range of H_2O spatial variation.
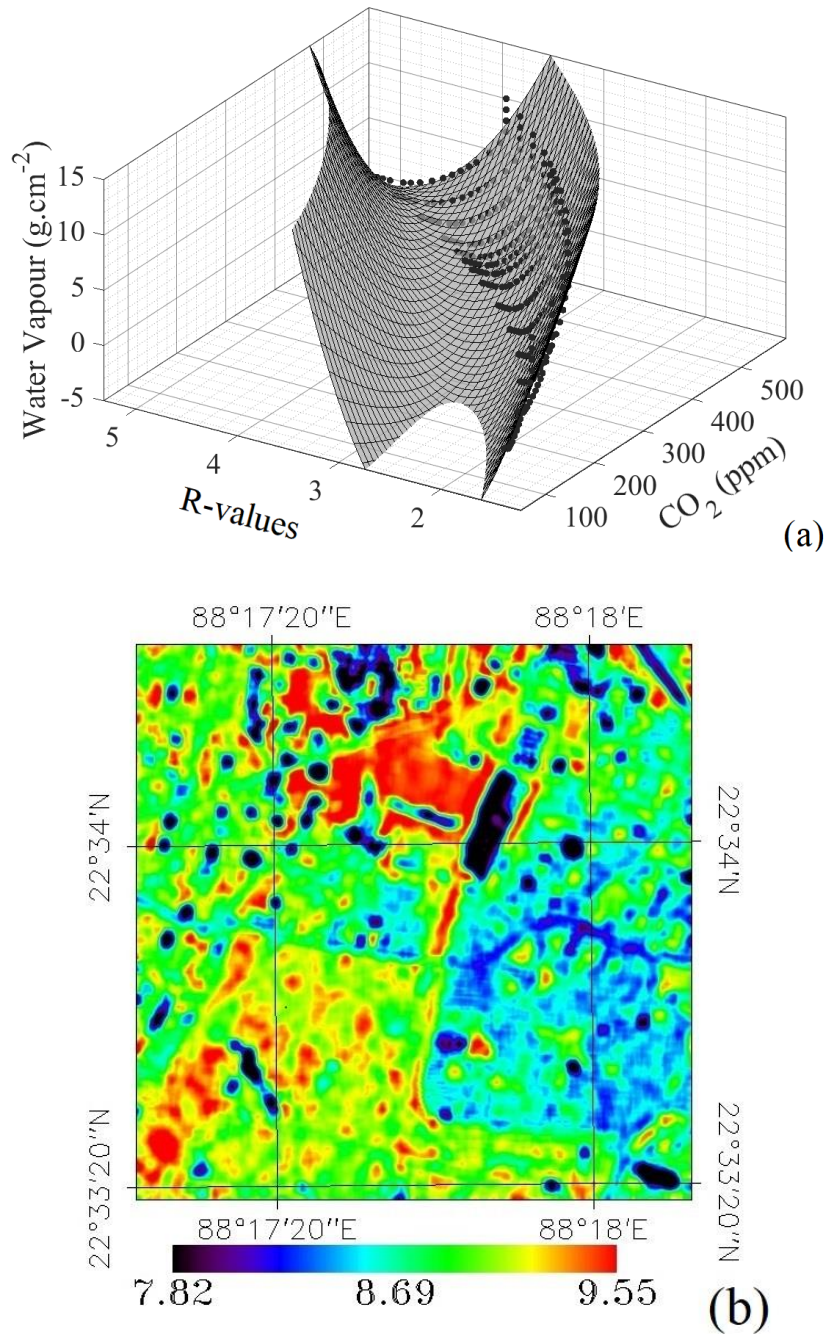
Figure 4. 8. Atmospheric water vapour (H_2O) concentration derived from the ratio (R) of the two CO_2 absorption bands: (a) The influence in R-values of CO_2 and H_2O change in grey mesh across vast ranges simulated using MODTRAN6 is shown in black dots, (b) the original H_2O distribution supplied with the AVIRIS-NG image.
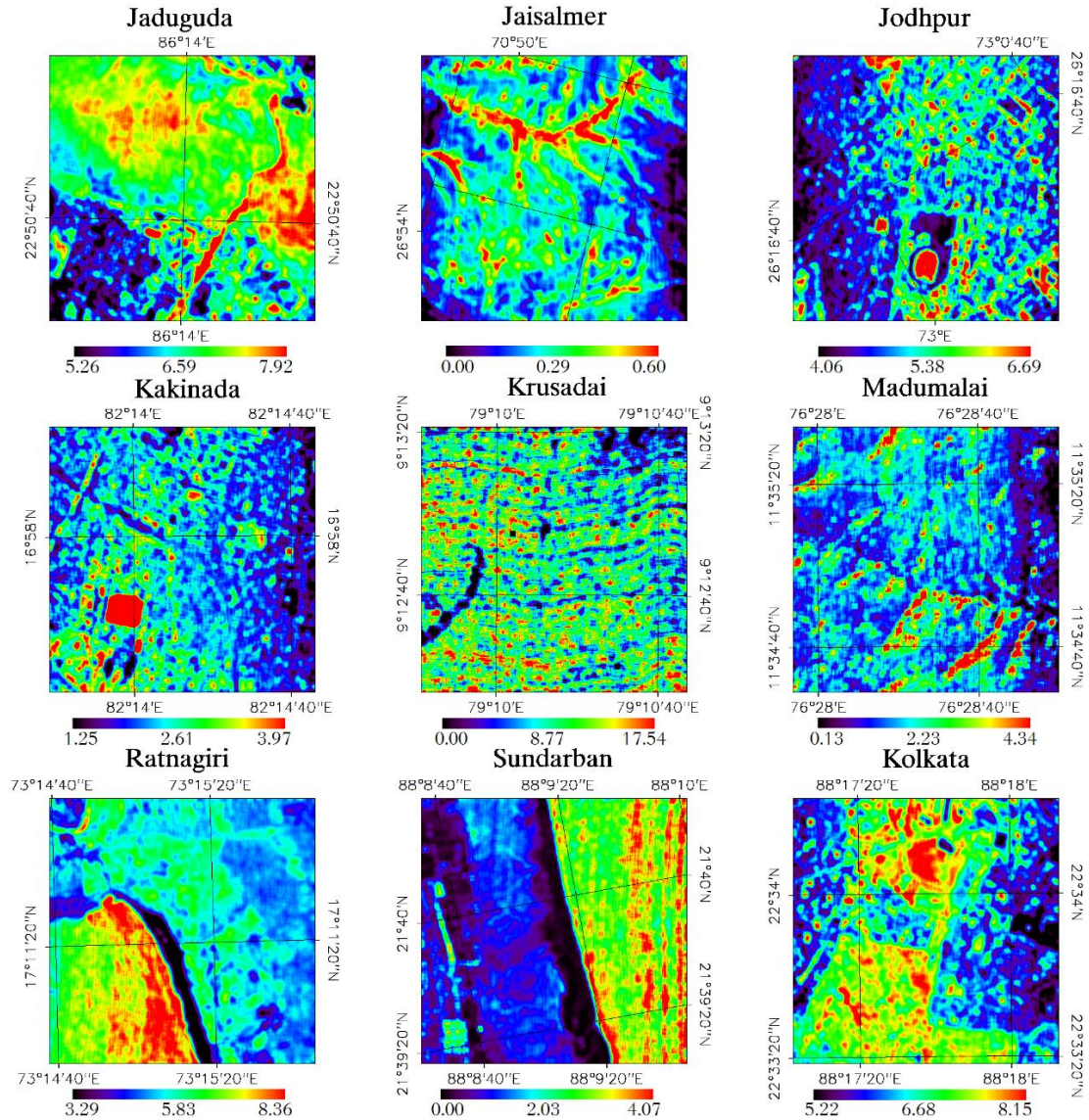
Figure 4. 9. Spatial distribution of H$_2$O (g cm–2) retrieved for all nine sites using the CO$_2$ and R values derived from AVIRIS-NG images.

4.7. Detecting Point Sources of CO$_2$

This section demonstrates that point sources of CO$_2$ can be detected from AVIRIS-NG images using the a-DOAS technique developed in section 3.1.3. A coal field region is expected to have a higher level of atmospheric CO$_2$ due to coal burns and other factors,

which differs from the overall increased CO$_2$ level in metropolitan areas. The approach is validated using images of Jharia coalfield areas centred at 23.78° N, 86.36° E.

Figure 4.10 depicts three distinct sections of the coal field area. The views acquired from Google Earth are compared to those received from AVIRIS-NG images. The geographical distribution of CO$_2$ concentration (ppm) obtained by the aforementioned approach is provided for all three areas. In all cases, significantly greater CO$_2$ concentrations are observed, which are grouped in a specific location. Following the AVIRIS-NG and Google Earth images, these are identified as the actual coal field areas. Figure 4.11 shows a similar arrangement of images and CO$_2$ distributions in conventional metropolitan areas near coal fields. The CO$_2$ concentration is not so localised here, but rather dispersed across the entire region. When the results of Figure 4.11 and Figure 4.10 are compared, it is clear that the present method is capable of estimating the spatial CO$_2$ distribution over widely varying surface features of contrast objects, such as waterbody and vegetation, and of identifying point sources of CO$_2$ with localised enhancement.

With Figure 4.12, which displays the difference in CO$_2$ concentrations at each pixel of the coal field region [Figure 4.10(a)] and the surrounding urban area [Figure 4.11(a)], the existence of the coal field as a point source of CO$_2$ becomes more prominent. When the individual spatial CO$_2$ distributions in these two locations are compared, it is clear that the higher CO$_2$ cluster is in the same location and spans almost the same distance as that of the actual coal field. It approves that the current approach can distinguish a specific CO$_2$ source from the general enhanced CO$_2$ levels caused by urban congestion.
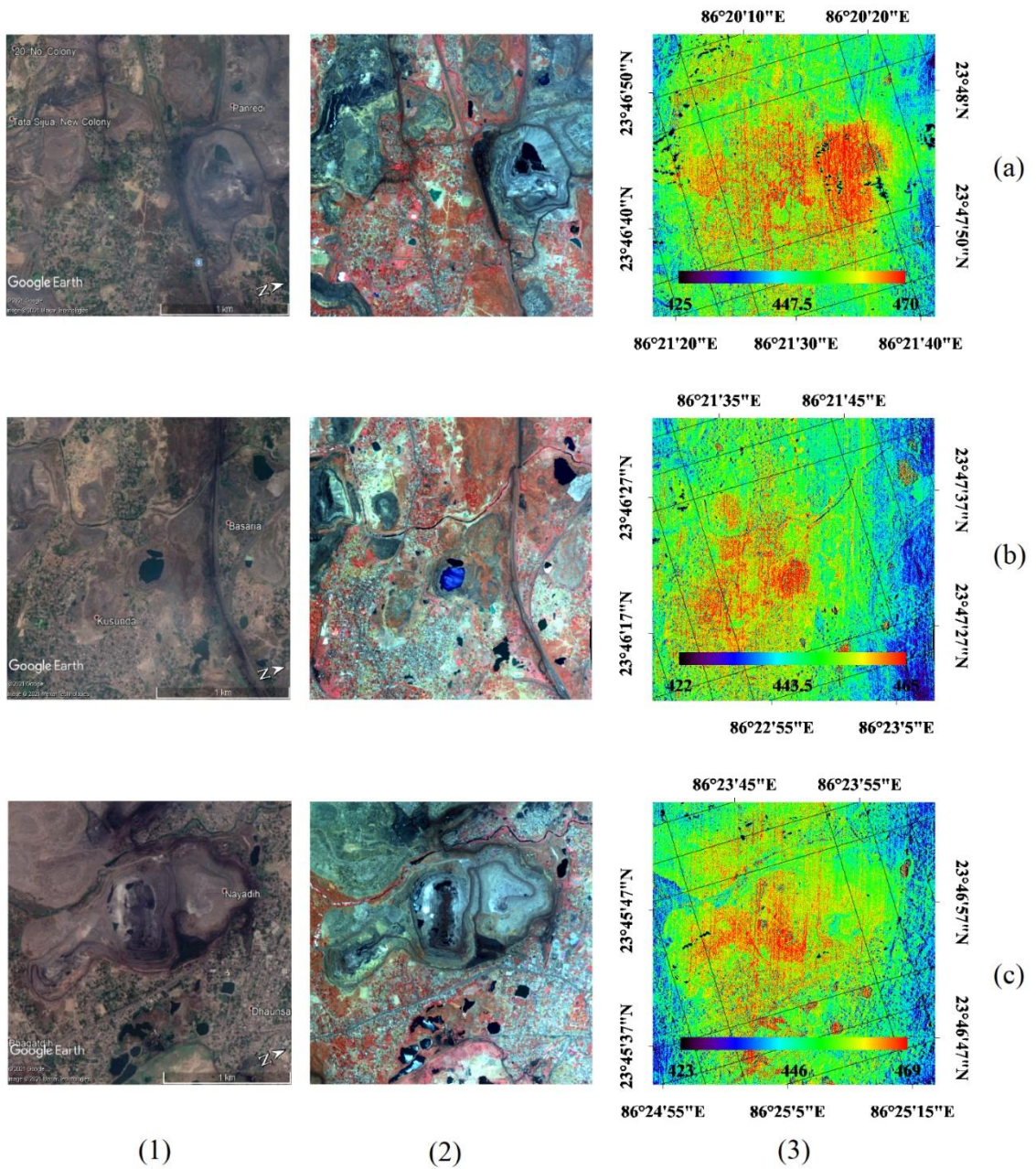
Figure 4. 10. Three separate sections of the coal field area (a), (b), and (c) with (1) the matching Google Earth picture, (2) the AVIRIS-NG false colour image segment, and (3) the corresponding spatial distribution of CO$_2$ concentration (ppm).
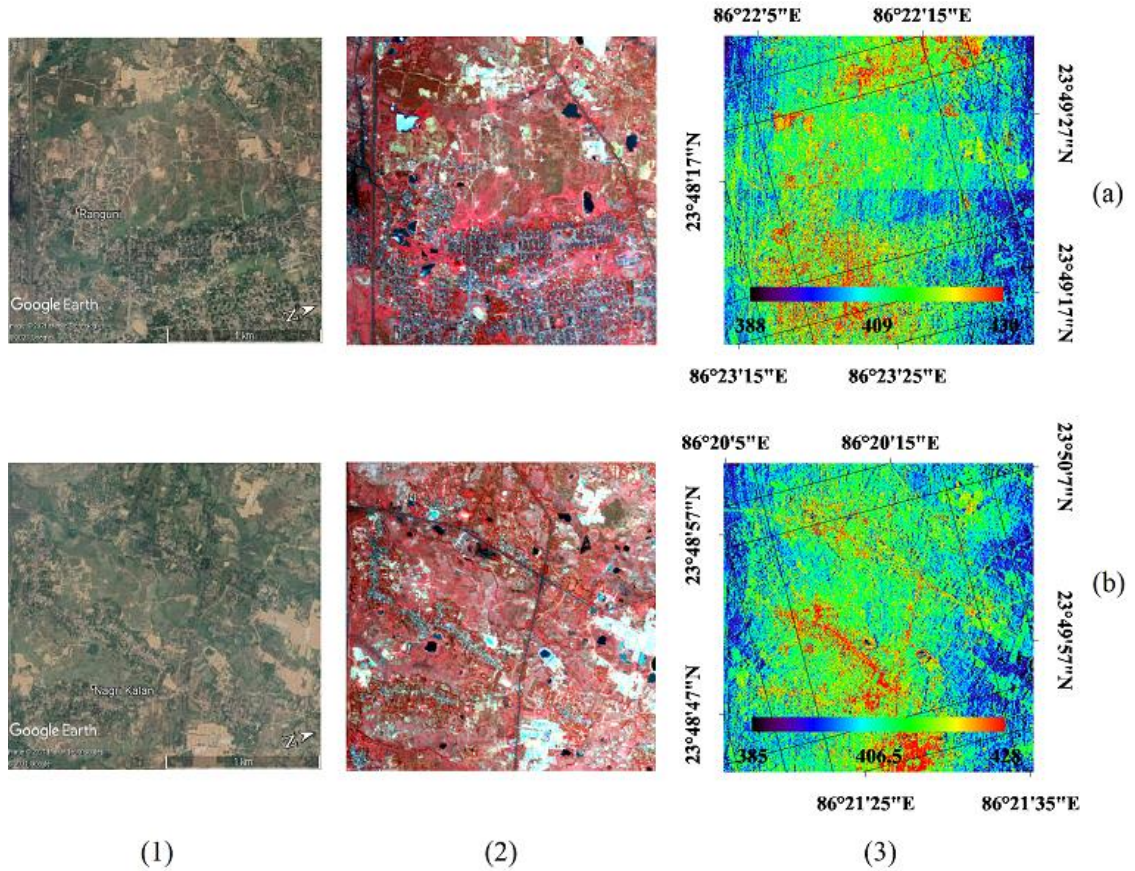
Figure 4. 11. Two separate locations (a) and (b) of the coalfield's (Figure 4.9) surrounding urban area are depicted with (1) the matching Google Earth picture, (2) the AVIRIS-NG false colour image segment, and (3) the related spatial distribution of CO$_2$ concentration (ppm).
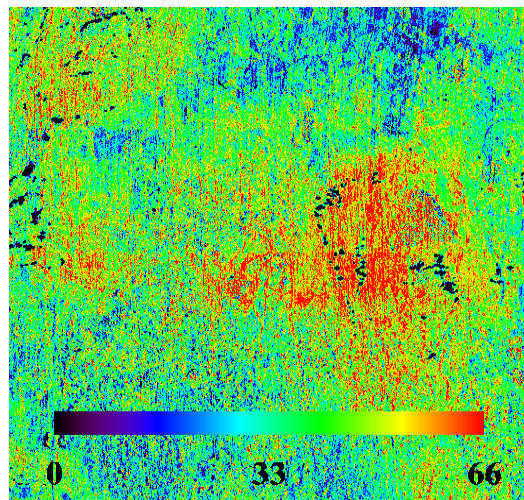

Figure 4. 12. CO$_2$ difference (ppm) between the coal field region [Figure 4.10(a)] and the surrounding urban area [Figure 4.11(a)].

The position of the CO_2 source may be more precisely pinpointed with further image post-processing, as seen in Figure 4.13. According to Figure 4.10, CO_2 concentrations in practically all of the locations surrounding the coal field are much higher than the current global average of roughly 410 ppm. A sufficient threshold CO_2 level can be assumed to distinguish such a zone from ordinary metropolitan regions, such as those depicted in Figure 4.11. In this situation, it is supposed that it is 10% higher than the world average and round it to 450 ppm. As seen in Figure 4.13, all of the sections in Figure 4.10 with CO_2 levels over this threshold are sorted out. These can provide a more precise outline of the high CO_2 zones.
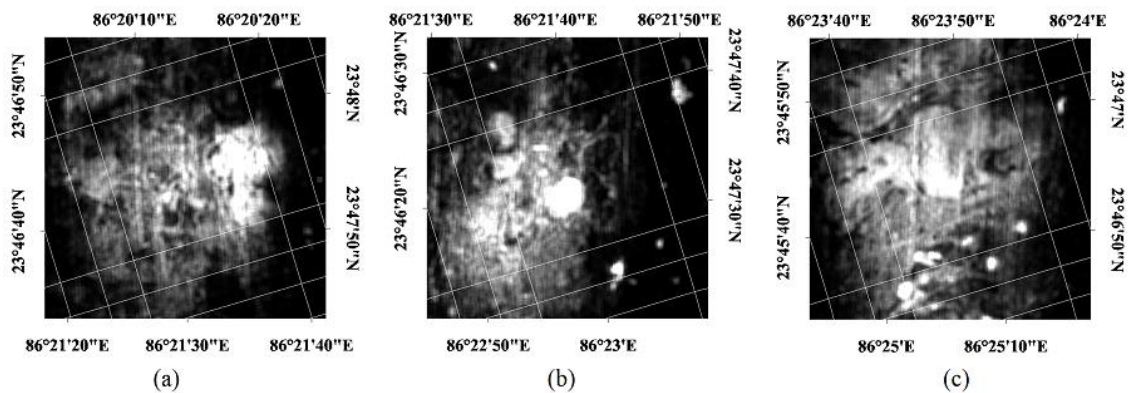

Figure 4. 13. Exact delineation of high CO_2 zones (white regions) utilising picture post processing and a threshold value of 10% higher than the world CO_2 average, rounded to 450 ppm. Figures 4(a), (b), and (c) correspond to Figures 1(a), (b), and (c).

Another useful potential of a method like the present one is explained with Figure 4.14, which shows the xCO_2 values procured by the global sensor OCO-2 in 2018 for the two previously described regions containing the coal field (Jharia) and the Kolkata-Howrah metropolitan areas (Kol-Hwh). It is worth noting that the total CO_2 concentrations in these two locations remain confined within the same range of 400 – 415 ppm whereas the true concentration in the coal field region is substantially higher, about 425 – 470 ppm (Figure 4.10). The presence of a major CO_2 source is thus averaged out in the worldwide monitoring system because of its coarse spatial resolution (1 km $\times$ 2 km). The

97

identification of any single local change necessitates an improved spatial resolution in observations such as this one.
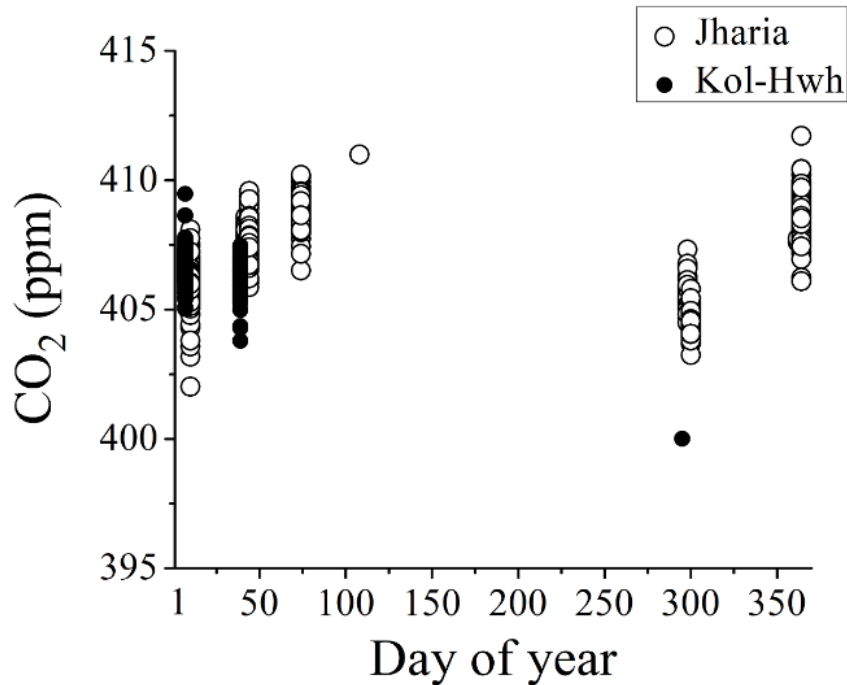

Figure 4. 14. The xCO$_2$ values procured by OCO-2 in 2018 for the regions around the coal field (Jharia) and the Kolkata-Howrah metropolitan areas.

4.8. Inferences

This work has retrieved the spatial variations of air-mixed CO$_2$ from the airborne hyperspectral images of AVIRIS-NG and has compared the findings with the contemporary results derived from OCO-2 database. The long-time change of CO$_2$ was studied with the data obtained from two independent sources: one from OCO-2 and the other from NASA Giovanni. A steady increase rate of the average CO$_2$ concentration over the major portion of Indian atmosphere and a balance of emission and sequestration are noted.

Mixing up of diversified surface features and maintenance of an equilibrium of emission and sequestration are inferred. This also highlights the important role of the large extent of vegetation distributed throughout India compensating for the anthropogenic

emission and holding a steady state in the increase of atmospheric CO$_2$.

Also, a useful methodology is put forward to estimate the spatial distribution of atmospheric H$_2$O, an important component of tropical climate like that of India. It is demonstrated that knowing the CO$_2$ and *R*-values (ratio of two absorption depths, illustrated in section 3.5) for each pixel of the image, the corresponding H$_2$O values can be derived.

Utilizing the high spatial resolution of AVIRIS-NG images and applied the *a*-DOAS methodology, this work has been able to detect CO$_2$ point sources and has validated the same with the results obtained from the images of Jharia coalfield area.

It is worth noting that this approach is to extract the absorption spectra of an atmospheric trace gas from a hyperspectral picture and estimate the gaseous concentration from the absorption depth using the gas's absorption cross-section. The approach was tested using CO$_2$ and proved to be helpful in recognising a specific source of CO$_2$. The approach was precise enough to discriminate between a localised source of CO$_2$ and an elevated CO$_2$ level in metropolitan regions. Because the approach is generic and based on a specific wavelength-dependent absorption property of a specific gaseous species, the same procedure should be applicable to the detection of any other greenhouse gas, such as methane, provided its absorption parameters are known. With a single case study, the current approach assures the detection of a local CO$_2$ source. If a similar technique were carried out at multiple locations at different times using a hyperspectral image sensor mounted on a more portable platform, such as a drone, a time series database on local CO$_2$ variations might be built up. Networking that database, as is done with aerosol data (Holben et al. 1998), may allow for the development of an IoT for smart monitoring of greenhouse gases.

Chapter References

Bhattacharya, B., Green, R., Rao, S., Saxena, M., Sharma, S., & Ajay Kumar, K. et al. (2019). An Overview of AVIRIS-NG Airborne Hyperspectral Science Campaign Over India. *Current Science*, *116*(7), 1082. doi: 10.18520/cs/v116/i7/1082-1088

Chapman, J. W., Thompson, D. R., Helmlinger, M. C., Bue, B. D., Green, R. O. & Eastwood, M. L. et al. (2019). Spectral and Radiometric Calibration of the Next Generation Airborne Visible Infrared Spectrometer (AVIRIS-NG). *Remote Sensing*, 11(18), 2129. doi: 10.3390/rs11182129

Dennison, P. E., Thorpe, A. K., Pardyjak, E. R., Roberts, D. A., Qi, Y. & Green, R. O. et al. (2013). High spatial resolution mapping of elevated atmospheric carbon dioxide using airborne imaging spectroscopy: Radiative transfer modeling and power plant plume detection. *Remote Sensing of Environment*, 139116-129. doi: 10.1016/j.rse.2013.08.001

Green, R. (2001). *Measuring the spectral expression of carbon dioxide in the solar reflected spectrum with AVIRIS*. Presentation, Proceedings of the 11th annual Airborne Earth Science Workshop, Jet Propulsion Laboratory, California Institute of Technology, Pasadena, California 91109.

Green, R. O. & Team, C. (2017). New measurements of the earth's spectroscopic diversity acquired during the aviris-ng campaign to India. *2017 IEEE International Geoscience and Remote Sensing Symposium (IGARSS)*, doi: 10.1109/igarss.2017.8127646

Green, R. O., Eastwood, M. L., Sarture, C. M., Chrien, T. G., Aronsson, M. & Chippendale, B. J. et al. (1998). Imaging Spectroscopy and the Airborne Visible/Infrared Imaging Spectrometer (AVIRIS). *Remote Sensing of Environment*, 65(3), 227-248. doi: 10.1016/s0034-4257(98)00064-9

Holben, B., Eck, T., Slutsker, I., Tanré, D., Buis, J., & Setzer, A. et al. (1998). AERONET—A Federated Instrument Network and Data Archive for Aerosol Characterization. Remote Sensing of Environment, 66(1), 1-16. doi: 10.1016/s0034-4257(98)00031-5

Raychaudhuri, B. & Roy, S. (2020). Investigation of seasonal variability of atmospheric columnar CO$_2$ over India in relation to environmental parameters using OCO-2 observation and vertical redistribution model. *International Journal of Remote Sensing*, 42(4), 1450-1473. doi: 10.1080/01431161.2020.1832281

Raychaudhuri, B. & Roy, S. (2022). A Proof of Concept for Estimating the Annual Atmospheric Carbon Dioxide Variation from Orbiting Carbon Observatory-3 vEarly Data. *IEEE Geoscience and Remote Sensing Letters*, 191-5. doi: 10.1109/lgrs.2021.3099172

Raychaudhuri, B. and Roy, S. (2021). Martian Atmospheric Spectral Radiance Used as Model for Water Vapor Correction of Terrestrial Carbon Dioxide Absorption Profile Around 2 μm. *IEEE Geoscience and Remote Sensing Letters*, 18(10), pp.1693-1697. doi: 10.1109/LGRS.2020.3007378.

Spinetti, C., Carrère, V., Buongiorno, M. F., Sutton, A. J. & Elias, T. (2008). Carbon dioxide of Pu`u`O`o volcanic plume at Kilauea retrieved by AVIRIS hyperspectral data. *Remote Sensing of Environment*, 112(6), 3192-3199. doi: 10.1016/j.rse.2008.03.010

Thorpe, A. K., Frankenberg, C., Thompson, D. R., Duren, R. M., Aubrey, A. D. & Bue, B. D. et al. (2017). Airborne DOAS retrievals of methane, carbon dioxide, and water vapor concentrations at high spatial resolution: application to AVIRIS-NG. *Atmospheric Measurement Techniques*, 10(10), 3833-3850. doi: 10.5194/amt-10-3833-20